Atmospheric vertical profiles of O_3, N_2O, CH_4, CCl_2F_2, and H_2O retrieved from external-cavity quantum-cascade laser heterodyne radiometer measurements

Tracy R. Tsai,[1] Rebecca A. Rose,[2] Damien Weidmann,[2,*] and Gerard Wysocki[1]

[1]Electrical Engineering Department, Princeton University, Princeton, New Jersey 08544, USA

[2]Space Science & Technology Department, Rutherford Appleton Laboratory, Harwell Oxford Campus,
Didcot, Oxfordshire OX11 0QX, UK

*Corresponding author: damien.weidmann@stfc.ac.uk

Received 17 August 2012; accepted 2 November 2012;
posted 12 November 2012 (Doc. ID 174523); published 20 December 2012

Atmospheric vertical profiles of ozone, nitrous oxide, methane, dichlorodifluoromethane, and water are retrieved from data collected with a widely tunable external-cavity quantum-cascade laser heterodyne radiometer (EC-QC-LHR) covering a spectral range between 1120 and 1238 cm^{-1}. The instrument was operated in solar occultation mode during a two-month measurement campaign at Rutherford Appleton Laboratory in Oxfordshire, UK, in winter 2010/2011, and ultrahigh-resolution (60 MHz or 0.002 cm^{-1}) transmission spectra were recorded for multiple narrow spectral windows (~1 cm^{-1} width) specific to each molecule. The ultrahigh spectral resolution of the EC-QC-LHR allows retrieving altitudinal profiles from transmission spectra that contain only few (1–3) significant absorption lines of a target molecule. Profiles are validated by comparing with European Centre for Medium-Range Weather Forecasts operational atmospheric profiles (ozone and water), with other data in the literature (nitrous oxide, methane, dichlorodifluoromethane), and with retrievals from a lower resolution (600 MHz or 0.02 cm^{-1}) Fourier transform spectroscopy data that were also recorded during the measurement campaign. © 2012 Optical Society of America

OCIS codes: 300.6310, 280.4991, 140.5965, 120.0280.

1. Introduction

Monitoring of the global distribution of atmospheric constituents is extremely important for better understanding of radiative forcing, transport, chemistry, and mixing effects in the atmosphere. Thermal infrared spectral sounding in the 3–5 and 8–12 μm atmospheric windows, where atmospheric trace gases exhibit strong fundamental rovibrational bands, is an effective method already widely used in currently operating passive remote sounding instruments [1]. Quantum-cascade laser heterodyne radiometry (QC-LHR) offers the potential for the development of extremely compact and lightweight thermal infrared sounders that combine high spectral resolution (<100 MHz or 0.003 cm^{-1}), high spatial resolution due to coherent field of view (FOV), and high sensitivity (ideally close to shot-noise-limited operation) [2,3].

Early LHRs used carbon dioxide gas lasers or lead salt lasers as the mid-infrared (mid-IR) local oscillators (LOs) and successfully targeted atmospheric ozone (O_3), nitrous oxide (N_2O), and methane (CH_4) [4–9]. However, carbon dioxide lasers are rather large laser sources that can only be frequency tuned in a discrete manner, thus limiting the number and type of molecules that can be observed with a

---

1559-128X/12/368779-14$15.00/0

single instrument. Although lead salt lasers are continuously tunable and could mitigate some of the gas laser technology shortcomings, they suffer reliability issues, require liquid nitrogen cooling, often exhibit multimode behavior, and provide low optical power. The advent and progress in quantum-cascade laser (QCL) technology have provided reliable, compact, and efficient mid-IR laser sources delivering several milliwatts of optical power with high spectral purity without the need for cryogenic cooling. These advantages make the QCL an ideal candidate to be used as an LO in an LHR instrument, and over the last few years the concept of QC-LHR for atmospheric observation has been successfully developed [2,3,10,11]. Initial studies of a ground-based prototype QC-LHR instrument operated in solar occultation mode to target ozone at around 1030 cm^{-1} demonstrated the potential of such technology in altitudinal distribution measurements [2]. In recent studies, the QCL LO and solar radiation were both coupled into a hollow waveguide for optical mixing, illustrating the potential for instrument miniaturization that would enable deployment on a wide range of platforms for atmospheric observation [11].

Previous QC-LHR instruments have been limited to monitoring one or two molecules due to the narrow frequency range of the instrument defined by the spectral tuning range of distributed feedback QCLs ($\sim$10 cm^{-1} achieved by temperature tuning and only $\sim$1 cm^{-1} available by variation of injection current). Application of a broadly tunable external-cavity QCL (EC-QCL) as the LO in an LHR system has been investigated by several groups [10,12]. As reported in 2009, a broadband external-cavity QC-LHR (EC-QC-LHR) results in a total tuning range of $\sim$180 cm^{-1} [10]. With recent developments in designing broadband QCL gain profiles, EC-QCL tuning ranges of over 430 cm^{-1} are achievable, which enables access to an entire atmospheric transparency window [13–15].

This work reports on atmospheric remote observations of five trace gases using a widely tunable ground-based EC-QC-LHR, which operates between 1120 and 1238 cm^{-1}. The EC-QC-LHR records $\sim$1 cm^{-1} wide ultrahigh-resolution (60 MHz) atmospheric transmission spectra centered anywhere within the available 118 cm^{-1} spectral tuning range that gives access to five atmospherically important molecules.

The five atmospheric absorbers targeted are O_3, N_2O, CH_4, dichlorodifluoromethane (CCl_2F_2, commonly known as CFC-12) and water vapor (H_2O). All these target molecules play an important role in atmospheric science. Ozone is predominantly found in the stratosphere, where it forms the ozone layer that protects the biosphere from UVB radiation; much lower levels of ozone (approximately 10% of the total column) are found in the troposphere. Anthropogenic emissions have been shown to impact the distribution of ozone in both the stratosphere and the troposphere. In urban areas, emissions of nitric oxides (NO_x) and volatile organic compounds can result in photochemical smog and increase the concentration of ozone in the troposphere, which is detrimental to the human respiratory system [16]. Emissions of chlorofluorocarbons (CFCs), such as CFC-12, which is targeted in our measurements, deplete the ozone layer via a catalytic photochemical cycle reducing ozone to oxygen [17]. CFCs were banned under the Montreal Protocol, and the 20-year ban on CFC-12 reduced its concentration to $\sim$500 parts per trillion by volume (pptv) in the troposphere [18,19]. N_2O and CH_4 contribute to global warming and are therefore regulated under the Kyoto Protocol [20,21]. Both molecules also exhibit a uniform distribution throughout the troposphere. Although N_2O is found in smaller concentrations [$\sim$320 parts per billion by volume (ppbv)] compared to other greenhouse gases in the troposphere, it is a potent global warming molecule because of its particularly long lifetime (120 years) [22]. While N_2O is rather inert in the troposphere, its concentration begins to decrease in the stratosphere due to photodissociation [23]. Similarly to N_2O, CH_4 has a relatively long lifetime ($\sim$12 years), which results in a uniform distribution throughout the troposphere [$\sim$1.8 parts per million by volume (ppmv)] [24]. Only in the stratosphere do CH_4 concentrations begin to decrease due to both slow vertical transport and stratospheric methane sinks (i.e., reactions with OH) [25,26]. Water vapor plays a crucial role in lower troposphere thermodynamics and weather systems [22,27]. Because changing atmospheric concentrations of these five target molecules affect the climate significantly, monitoring of these molecules is of great importance to both atmospheric scientists and to policy makers.

A measurement campaign was carried out at Rutherford Appleton Laboratory in Oxfordshire, UK (−1.31° longitude and 51.57° latitude) during December 2010 and January 2011 with the aim of demonstrating the capabilities of the EC-QC-LHR instrument and comparing its performance with a commercial high-resolution Fourier transform spectrometer (FTS). Atmospheric spectra of the five target molecules were recorded, and preliminary raw spectra from this campaign were presented in Ref. [28]. An extended retrieval analysis of these campaign data is hereby presented. Vertical profiles of O_3, N_2O, CH_4, CFC-12, and H_2O are retrieved from the acquired spectral data. These profiles are compared against data from the literature and also against profiles retrieved from FTS measurements acquired during the same measurement campaign, and the potential advantages of the EC-QC-LHR instrument are discussed.

2. Experimental Details

A. Instrument Configuration and Operation Principle

The optical arrangement and the technical details of the instrument have already been described in Ref. [28], and therefore only a brief overall description of the optical system arrangement is summarized here.

The LO is an EC-QCL tunable between 1120 and 1238 cm^{-1}. The Littrow-based EC-QCL configuration and operation principle have been described in detail previously [29]. The laser can be coarsely tuned to any wavelength within the tuning range. Then a high-resolution mode-hop-free scan of $\sim 1\ \text{cm}^{-1}$ (limited by the QCL chip's current dynamic range from threshold to rollover) can be performed using a piezo-actuated cavity tuning system synchronized with the laser current scan. The mode-hop-free tuning is performed with a sinusoidal waveform to avoid excitation of higher-order mechanical vibrations in the piezo-actuated optomechanical cavity system. The LO power is controlled via polarizer to provide the optimum heterodyne signal and prevent detector saturation. A 25R/75T beam splitter is used as a mixing plate to combine the LO with the collected thermal (solar) radiation. The 25% reflected LO intensity is imaged onto a square law detector, a high-speed (1 GHz) mercury cadmium telluride photodetector used as a photomixer. The 75% of transmitted LO intensity is used for frequency diagnostics: a flip mirror directed the LO radiation either to a wavemeter (Bristol 721) for absolute frequency calibration or to a 1 in. (25.4 mm) germanium etalon followed by a photodetector to record relative frequency calibration signals.

The solar radiation is captured by a heliostat, which actively tracks the apparent location of the sun. An aperture stop limits the FOV to retain only the spatially coherent field contributing to the heterodyne mixing process. The corresponding FOV was measured to be ~5.2 arcmin, equivalent to viewing 1/38th of the solar disc. The solar radiation is directed into the laboratory and passed through an optical filter that transmits wavelengths longer than 7 μm and reflects shorter wavelengths onto a broadband (800–1750 μm) large-area germanium detector to monitor the intensity of the solar radiation. Radiation with wavelengths >7 μm is first modulated by a chopper at 1.8 kHz and then superimposed with the LO beam using the aforementioned 25R/75T mixing plate.

The solar radiation transmitted through the Earth's atmosphere contains information about absorbing constituents. The heterodyne process downconverts the spectral information from the mid-IR to the radio-frequency (RF) domain. The AC output of the photomixer provides the spectral information while the DC output offers a means to monitor the LO power. The RF signal is amplified by two 30 dB amplifying stages and filtered by a 10–40 MHz bandpass filter, which defines the instrument lineshape (ILS) that results in a 60 MHz double-sideband spectral resolution of the radiometer. The RF signal power is detected by a zero-bias Schottky diode (Herotek DX401), and its output is demodulated by a lock-in amplifier (Ametek model 7265) at the chopper frequency (1.8 kHz).

In a small subset of measurements aiming to compare the EC-QC-LHR with a high-resolution FTS (IFS Bruker 125HR) with the same FOV (the same spatial resolution), a 50/50 beam splitter was introduced in the optical path of the solar radiation to perform simultaneous measurements with both instruments. These measurements are discussed in Section 5.

B. Data Acquisition and Processing

LabView software was developed to control the instrument and acquire data. The software performs wavelength tuning of the EC-QCL and records five data streams: the in-phase and quadrature components of the lock-in demodulated heterodyne signal, the DC signal of the photomixer for LO power tracking, the transmission spectrum of a germanium etalon for frequency calibration, and the recorded solar power. To ensure adjacent data points are uncorrelated, data points are acquired every 2.5 times the lock-in time constant (τ), which resulted in scan times between 1 and 12 min, depending on the τ chosen. Postprocessing of the raw experimental data is required to obtain the heterodyne transmission spectrum of the atmosphere as summarized in Fig. 1.

In the postprocessing, the lock-in reference phase was numerically rotated to maximize the spectral signal in the in-phase component. The in-phase signal retained an offset due to residual thermal contrast, which was subtracted. Because the power of the RF heterodyne signal is proportional to the LO power and the solar power, both parameters were monitored and used in the postprocessing. The tuning of the QCL bias current (required for mode-hop-free tuning) results in significant changes in the LO power during a single spectral scan. This produces a baseline variation that is factored out through power normalization in postprocessing. Small solar power variations were also corrected, but significant changes ($>10\%$ of the average signal) in measured solar intensities due to cloud cover were difficult to correct for. If those large fluctuations were easily distinguishable from the spectroscopic features, the raw spectra were truncated so that the effects of the large solar power fluctuations were excluded. If large solar power fluctuations occurred throughout the scan, the data was discarded and not considered for further analysis.

The scan frequency axis was calibrated using a 1 in. (25.4 mm) germanium etalon with a free spectral range of 0.0492 cm^{-1}. After mapping all transmission peaks and valleys, an algorithm determined a fifth-order polynomial equation for frequency calibration. Although the laser was tuned with a sinusoidal waveform, due to small tuning nonlinearities a high-order polynomial was more accurate in describing the wavelength tuning characteristics than a simple sinusoid. The absolute frequency was set using a single absorption feature appearing within the spectra simulated for standard mid-latitude atmospheric conditions at zenithal

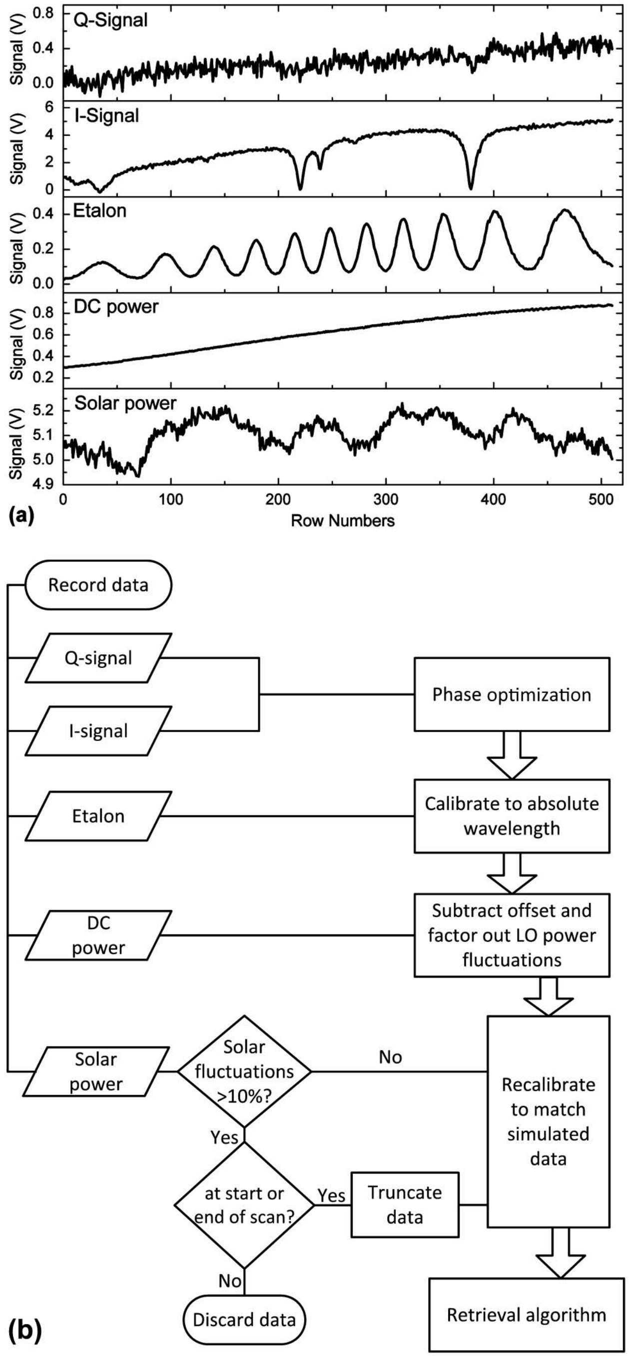

Fig. 1. (a) Raw signals acquired during a single spectral scan and (b) flow diagram of data postprocessing. Q and I signal represent the quadrature and in-phase lock-in signal, respectively.

elevations. Experimental measurements additionally revealed a systematic ~1.1% discrepancy in frequency calibration. By taking into account uncertainties specified by the manufacturer for the etalon length, laboratory temperature fluctuations (affecting the etalon length through thermal expansion), and optical dispersion, the free spectral range is accurate to 16.4 MHz (or 0.00055 cm^{-1}), which corresponds to 1.14% in the relative frequency scale and is on the order of the observed discrepancy. As a result, to account for the systematic calibration errors, after the etalon calibration and baseline corrections steps, a single stretch parameter was used to fine-tune the frequency axis and match spectral line positions obtained from the HITRAN 2008 database [30]. Because each spectral window contains more than three absorption features, a linear regression yields a strong fit.

3. Atmospheric Profile Retrieval Method

A. Optimal Estimation Method

Retrievals were performed using the optimal estimation method (OEM), the principles of which were described in detail by Rodgers [31], and the approach applied to atmospheric heterodyne spectra was described [2]. In summary, the inverse problem is described in Ref. 2

$$y = F(x) + \varepsilon, \tag{1}$$

where y is the measurement vector (spectra produced by the instrument), x is the state vector of parameters to retrieve, and ε is the measurement error vector. F is the physical model describing the instrumental output by taking into account the atmospheric transmission and the instrumental parameters. The atmospheric transmission is calculated using the reference forward model (RFM) [32], which simulates atmospheric transmission based on experimental parameters, atmospheric conditions, and spectral line parameters from the HITRAN 2008 database. The RFM is fed with temperature and pressure profiles obtained from the European Center for Medium-Range Weather Forecasts (ECMWF) [33], which were then interpolated from the latitude, longitude, and time grids to match the exact location and time of the measurements reported in this work. The model of the instrument includes noise performance, gain, and the ILS function. The parameters in the state vector (x) retrieved were the volume mixing ratios (VMRs) at a preselected altitude grid and coefficients of a second-order polynomial baseline used in the model to account for heterodyne gain variation and nonselective absorbers (e.g., aerosols) within the spectral window. The natural logarithm of VMR was taken to constrain the VMR to only positive values as well as to allow for wide dynamic range.

To solve for x in Eq. (1), the OEM uses an iterative Levenberg–Marquardt approach to minimize the cost, χ^2, which is a measure of the convergence of the fit with the data and the *a priori* knowledge as described in the following equation:

$$\begin{aligned}\chi^2 = {} & (y - F(x_n))S_\varepsilon^{-1}(y - F(x_n))^T \\ & + (x_a - x_n)S_a^{-1}(x_a - x_n)^T,\end{aligned} \tag{2}$$

where S_ε is the measurement covariance matrix, S_a is the *a priori* covariance matrix, x_a is the *a priori* parameter vector, and x_n is the state vector at the nth iteration. The *a priori* VMRs are taken from a typical mid-latitude atmospheric profile compiled for retrievals from the Michelson Interferometer for Passive Atmospheric Sounding (MIPAS) satellite [32] data, interpolated at a preselected altitude grid. The *a priori* baseline values for the offset and polynomial coefficients are 1.5 and 0.5 times the maximum in-phase signal, respectively. The *a priori* covariance matrix is a diagonal matrix set to 100% error in *a priori* retrieval concentrations, 50% error in baseline offset, and 1000% error in higher-order baseline polynomial coefficients. The measurement covariance matrix is also a diagonal matrix that is set to match the ideal shot-noise limit of the instrument scaled by the instrument degradation factor (defined as the ratio of experimental detection limit to the ideal shot-noise-limited case as described in [28]). Typical degradation factors for this instrument were within a range of 20 to 28. In the retrievals, the best-case-scenario degradation factor of 20 is used. In a well-conditioned retrieval, the cost divided by the number of data points should be close to unity, and the deviation from unity indicates an incorrect estimation of instrument noise or errors in the forward model.

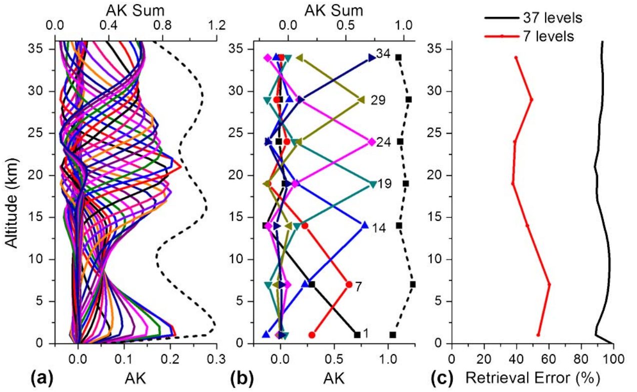

Fig. 2. (Color online) Prior analysis data used for optimization of the altitude grid. AKs for the retrieval of ozone between 1129.90 and 1130.30 cm^{-1} resulting from (a) 0–36 km altitude grid with 1 km spacing, (b) an optimized seven-level altitude grid. The black dotted lines indicate the sum of the AK elements at each altitude (top axis), and in (b) the number labels indicate the altitude associated with each AK peak, and (c) shows a comparison of percentage retrieval errors estimated for the two altitudinal grids.

B. Prior Analysis and Altitude Grid Definition

Before performing a complete analysis, single-iteration retrieval for an ideal instrument was performed for each molecule in every spectral window to define the optimum altitude grid providing the largest amount of vertical information with the smallest retrieval error. The optimum altitude grid for each molecule within each narrow spectral window depends on the spectral resolution of the instrument, *a priori* values, the number of absorption lines, line strengths, line broadening parameters, and spectral interferences from other molecules. To determine the optimal altitude grid, calculations based on the prior analysis were first performed with an unrealistically dense altitude grid covering 0 to 36 km in 1 km steps. Analysis of the resulting averaging kernels (AKs) provides information about the retrieval: the width of the AK gives the vertical resolution of the instrument at the corresponding altitude, and the area under the AK (equivalently, the sum of the AK values over a given row) is proportional to the information retrieved from the measurement rather than *a priori*. Figure 2(a) presents the AKs for an ozone spectrum between 1129.90 and 1130.30 cm^{-1} calculated for the altitude grid with 1 km spacing. The AKs appear much broader than the simulated 1 km resolution of the input altitude grid, indicating that much of the retrieved information is redundant. Figure 3 shows the simulated spectrum, weighting function, and gain matrix of these dense grid calculations. The weighting function describes the sensitivity of the forward model to the state vector and demonstrates that, for the ozone absorption lines, sensitivity is greatest at the wings (within a narrow range from the line center) at stratospheric altitudes between ~12 and ~32 km, which is consistent with the highest concentrations of ozone expected at high altitudes. The gain matrix shows the sensitivity of the retrieved concentrations to the measurement vector, and Fig. 3(c) demonstrates that the measurement vector contributes the most information within a relatively narrow range in the wings of the absorption lines and at altitudes above about 12 km, which agrees well with the weighting function. Both the weighting function and the gain matrix show that the spectral line at 1130.11 cm^{-1} provides the most information at the highest altitudes. This is expected because the other two lines in the spectrum are more intense and nearly saturated, hence reducing sensitivity at the line center to the Doppler-limited measurement at high altitudes.

The optimized vertical resolution was selected based on the Rayleigh criterion for AK width and minimizing cross correlation between retrieved parameters. To maximize the amount of information retrieved from the measurement, an additional criterion was set: the area under the AKs must be within 15% of unity for each element of the state vector. Within these criteria, Fig. 2(b) shows the AKs calculated for the new optimized altitude grid chosen for ozone profiling. With this optimized altitude grid, the sum of the AKs meets the criteria, indicating that the information retrieved is relevant to the correct element of the state vector and provides high confidence in the retrieved values. This is further represented by Fig. 2(c), which shows how the optimization of the altitude grid reduces the retrieval error by approximately half. The optimized altitude grids for the five target molecules have been obtained with a similar prior analysis process. The chosen altitude grid as well as frequencies, line strengths, and absorption bands of the most significant spectral features in each of the four spectral windows investigated in this work are given in Table 1.

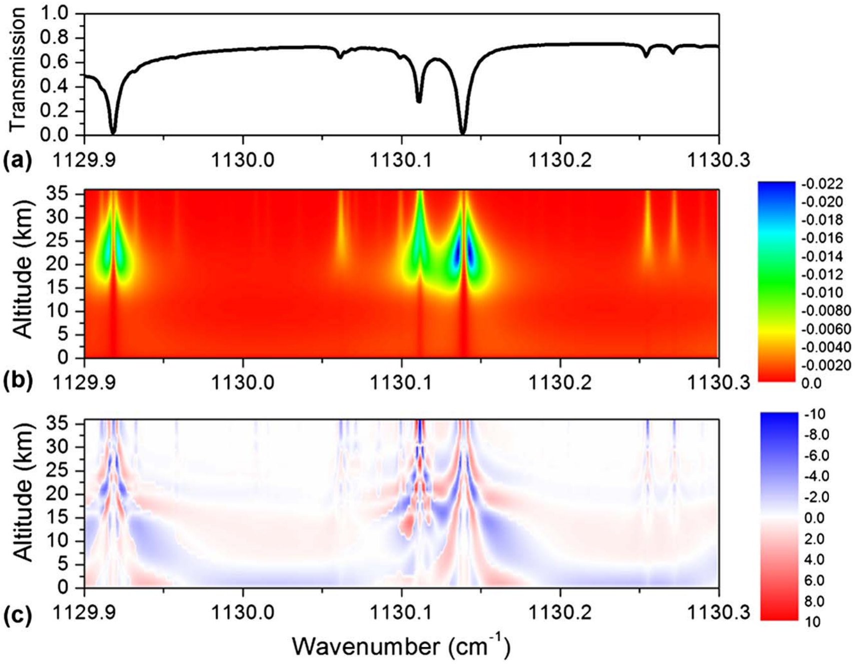

Fig. 3. (Color online) Prior analysis data for ozone in the spectral window between 1129.90 and 1130.30 cm^{-1} on a 1 km spaced grid covering 0 to 36 km: (a) is the simulated spectra, (b) is the weighting function, and (c) is the gain matrix. The color bar in (b) gives the values of the weighting function in units of ppmv^{-1} and in (c) gives the gain matrix values in units of ppmv with different colors indicating positive or negative gain. The oscillations in (c) are related to competing contributions of spectral channels with altitude caused by pressure and temperature atmospheric profiles.

4. Retrievals of Atmospheric Vertical Profiles

Retrieval results for each molecule obtained from spectral fitting performed in each optimized spectral window listed in Table 1 are presented in this section.

A. Ozone

The spectral window 1 chosen for ozone retrieval covers frequencies between 1129.90 and 1130.33 cm^{-1}. This spectral range includes three strong ozone absorption lines. Figure 4 shows the recorded heterodyne transmission spectrum, which has been frequency calibrated and processed as described in Section 2.B. The overlaid solid red line in the figure is the result of fitting to the experimental spectrum using the OEM retrieval algorithm described in Section 3 with the altitude grid defined in Table 1. The residuals plotted in Fig. 4 are randomly distributed and indicate a high-quality fit. The top plot of Fig. 4 shows RFM simulation of a standard atmospheric transmission for the purpose of molecular line identification. In spectral window 1 there is a broad water line that also contributes to the total absorption; therefore, the quality of the OEM fit was significantly improved when the concentration profile of water vapor was retrieved together with the ozone profile. The water vapor profile was retrieved on a two-point altitude grid of 1 and 3 km, as guided by prior analysis calculations.

Figure 5(a) shows the retrieved concentration profile of ozone overlaid with the ozone profile derived from ECMWF operational analysis interpolated in time and space to match the measurement timing and location [33]. The retrieved profile is in reasonably good agreement with the ECMWF profile at altitudes between 7 and 29 km, but at altitudes of 1 and 34 km the agreement is poor. The quality of this retrieval was carefully investigated by examining the resulting AKs shown in Fig. 5(b) and the retrieval error covariance. The AKs indicate that the retrieval is sensitive at levels between 14 and 29 km, but strongly reduced sensitivity is observed for O_3 at 1, 7, and 34 km. The retrieval shows almost no sensitivity at 1 km, where the area of the AK is close to zero, and the retrieval at 34 km is heavily cross correlated with the retrieval at 29 km (<29%). The reduction in the quality of the AKs coincides with the altitudes at which the retrieved profile is strongly inconsistent with the ECMWF profile. Additionally, the total column density of ozone obtained by integration of the vertical profile is 324 Dobson Unit (DU), which is 9.5% lower than the total column density of ozone obtained from ECMWF of 358 DU.

As discussed earlier, the profile of water is also retrieved at 1 and 3 km, and the concentrations returned are 6623 and 1411 ppmv, respectively. The AKs that correspond to the retrieval of the water vapor profile indicate little cross correlation with ozone and with the retrieved baseline parameters. The AKs suggest that reliable information can be retrieved about the water concentration at 1 km and less reliable information is retrieved at 3 km; the retrieval errors of the water profile are 31% at 1 km

Table 1. Main Target Absorption Lines within the Four Spectral Windows Selected for Atmospheric Profiling[a]

Molecule	Frequency (cm^{-1})	Intensity ($cm^{-1}/molec \cdot cm^{-2}$)	Band	Altitude Grid (km)	τ (ms)	Acquisition Time (s)
Spectral window 1: 19 January 2011, 10:16						
$^{16}O_3$	**1129.92**	**9.59E − 22**	**ν_1**	**1, 7, 14, 19, 24, 29, 34**	200	190
	1130.11	**1.62E − 22**	**ν_1**			
	1130.14	**1.06E − 21**	**ν_1**			
$H_2{}^{18}O$	1129.87	3.92E − 25	ν_2	1, 3		
Spectral window 2: 19 January 2011, 10:18						
$^{14}N_2{}^{16}O$	**1161.48**	**3.95E − 21**	**$2\nu_2$**	**1, 8, 15, 21**	100	91
CCl_2F_2[b]	**1161.07**	**1.04E − 19**	**ν_8**	**1, 8**		
$^{16}O_3$	1160.90	2.13E − 22	ν_1	2, 14, 26, 36		
	1161.01	9.52E − 23	ν_1			
	1161.27	3.06E − 22	ν_1			
	1161.29	3.18E − 22	ν_1			
Spectral window 3: 18 January 2011, 10:36						
$H_2{}^{16}O$	**1193.49**	**7.30E − 27**	**ν_2**	**0.5, 4**	200	181
$^{14}N_2{}^{16}O$	1194.04	3.13E − 21	$2\nu_2$	1, 9, 15, 22		
Spectral window 4: 28 January 2011, 13:17						
$^{12}CH_4$	**1216.20**	**3.32E − 21**	**ν_4**	**1, 8, 19**	100	109
	1216.24	**2.08E − 22**	**ν_4**			
	1216.33	**1.10E − 22**	**ν_4**			
	1216.63	**1.11E − 21**	**ν_4**			
$H_2{}^{16}O$	1216.19	3.70E − 25	ν_2	0.5, 3.5		

[a] Molecules shown in bold are the main targets in each spectral window selected to retrieve vertical profiles (molecules not shown in bold were still incorporated into the model to improve the quality of retrieval).

[b] The Q-branch of CF_2 stretch of CCl_2F_2 has many congested lines that formed one broadband absorption feature, and the table lists the strongest line and its center frequency. For more detailed information, please refer to Refs. [34,35].

and 88% at 3 km. These errors are reduced by analyzing a distinct water line, which will be discussed in Section 4.E.

To reduce the ozone retrieval errors, the retrieval error covariance is further studied. The retrieval errors are characterized by the measurement noise covariance, which results from random noise inherent to the measurements, and the smoothing error covariance, which describes the retrieval errors due to the finite vertical resolution of the observing system. The diagonal elements of these two covariance matrices and the sum (total error) are plotted in Fig. 5(a). At all altitudes the smoothing error is the dominant term, and the increase in smoothing error at 1, 7, and 34 km is primarily responsible for the increase in the total error at these altitudes, reflecting nonideal AKs.

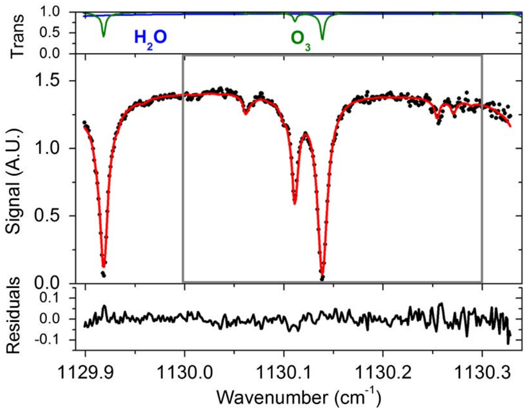

Fig. 4. (Color online) Spectral window 1. The top plot is an RFM simulation of the transmission spectrum for standard atmospheric conditions; the center plot is the experimental spectrum (black dots) with the OEM fit overlaid in red; and the bottom plot shows the residual differences between the OEM fit and the data. The gray box in the center plot indicates the truncated spectral range used for O_3 retrieval.

The retrieval errors shown in Fig. 5 are much larger than those from the prior analysis presented in Fig. 2. This is largely a result of an experimental measurement error that is two times larger than the measurement error assumed in the prior analysis simulations. The impact of the LO power variation on the retrieval analysis was also investigated. An OEM retrieval analysis was performed on an experimental spectrum that had not been corrected for LO power variation. In this retrieval the *a priori* baseline parameters are set equal to the coefficients of a second-order polynomial fit to the recorded LO power, and the *a priori* covariance is set to be diagonal with the variance in the zeroth-, first-, and second-order coefficients corresponding to 50%, 100%, and 100% uncertainty, respectively. The ozone profiles retrieved were the same (within the retrieval errors) as those retrieved from the LO power-corrected data, which confirms that no bias is introduced by this baseline correction method.

To minimize random noise in the retrieval errors, the gain matrix in Fig. 3(c) was further studied. The gain matrix indicates that the ozone line at 1129.92 cm^{-1} has high gain levels at high altitudes, which also represents high sensitivity to noise. Therefore this gain level must be balanced between the noise sensitivity and the sensitivity to information that can be retrieved based on the weighting function shown in Fig. 3(b). The weighting function

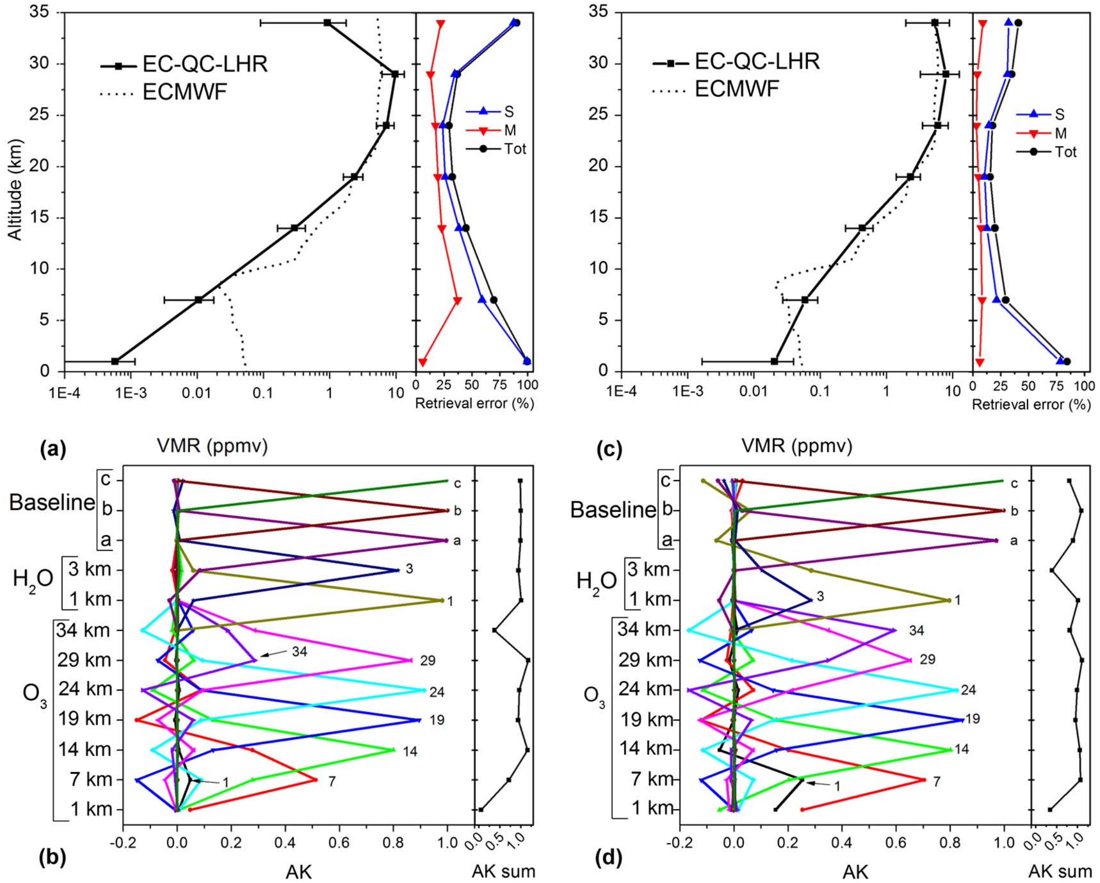

Fig. 5. (Color online) Retrieved profiles of ozone and resulting AKs after fitting using the OEM retrieval algorithm. (a) and (b) show, respectively the profiles and AKs obtained from the full spectral window 1, (c) and (d) show, respectively the profiles and AKs from a retrieval over a truncated range of 1129.99 to 1130.29 cm^{-1}. In (a) and (c) the retrieval error and profiles are plotted on a log scale and are compared to the ECMWF profiles (dashed line). Relative retrieval errors are plotted on the right of (a) and (c). The total retrieval error (Tot) includes the retrieval error from smoothing (S) and measurement noise (M). In (b) and (d) the sums of the AKs are indicated on the right plots.

clearly shows that the two ozone lines at 1130.11 and 1130.14 cm^{-1} are the most sensitive features to retrieve the information at high altitudes. Thus, in order to minimize retrieval noise, spectral window 1 has been truncated to the 1129.99 to 1130.29 cm^{-1} range. The retrieval performed for this spectral range is shown in Fig. 5(c). Compared to the full spectral range, the random measurement noise at 34 km obtained with the truncated window is reduced significantly from 22% to 8.8%. The smoothing error also decreases because the AK for 34 km, shown in Fig. 5(d), has a peak value closer to unity and is no longer heavily cross correlated with the retrieval at 29 km. Therefore, the total retrieval error at 34 km is reduced by almost half. As a result, the ozone concentration at 34 km shows better agreement with the ECMWF-generated profile at this altitude. The retrieval errors at 1 and 7 km have also improved: the AK peak value at 7 km increases by 40% compared to the peak value calculated for the full spectral window. The retrieved concentration at 1 km also agrees better with the ECMWF profile with the total error reduced from ~100% to ~85%. However, the low AK values and high smoothing error at 1 km still indicate that the retrieval at this low altitude is not well conditioned. This is consistent with the weighting function matrix that indicates significantly lower sensitivity at low altitudes. Because this truncated window includes less broadband information, the water and baseline AKs indicate more cross correlation between these retrieved values as expected. Nevertheless, AKs indicate no cross correlation between the water/baseline parameters and the ozone parameters. Therefore, the ozone retrievals can still be taken in good confidence above 1 km, and the retrieved concentrations above 1 km do not differ from the ECMWF profile by more than the calculated error bars. The total column density of ozone of 338 DU derived from the retrieved vertical profile is larger than the total column density derived from the full spectral window and shows an improved agreement to within 5.5% of ECMWF data.

B. Dichlorodifluoromethane

The Q branch of the ν_8 absorption band of CFC-12 corresponding to the CF_2 asymmetric stretch is observed at ~1161.0 cm^{-1}. It is a broadband absorption feature composed of many unresolved rovibrational

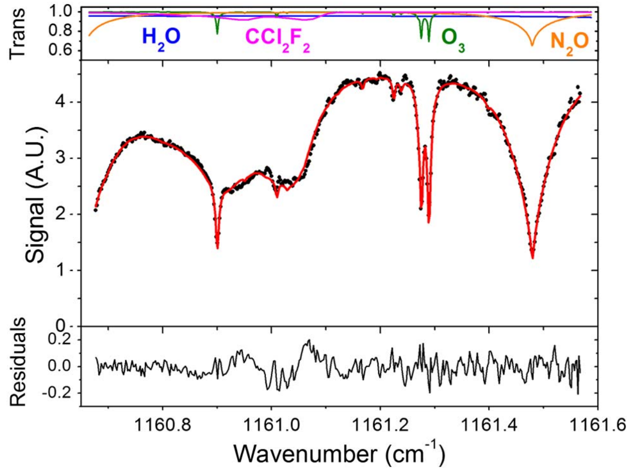

Fig. 6. (Color online) Spectral window 2. The top plot is an RFM simulation of the transmission spectrum for standard atmospheric conditions; the center plot is the experimental spectrum with the OEM fit overlaid; and the bottom plot shows the residual differences between the OEM fit and the data.

lines. Figure 6 shows an experimental spectrum recorded within a spectral window between 1160.68 and 1161.57 cm^{-1}, which in addition to the CFC-12 absorption also contains features attributed to O_3, N_2O, and H_2O. Because the CFC-12 feature is broadband, prior analysis shows that the vertical information is limited to the lower troposphere and yields only a two-point optimized vertical grid with 1 and 8 km altitude points. The optimized altitude grids for N_2O and O_3 in the same spectral range contain four altitude points with 1, 8, 15, and 21 km for N_2O (to be discussed in the next section) and 2, 14, 26, and 36 km for O_3. No advantage was found in retrieving a broadband water vapor profile in this spectral window, which was found to be strongly correlated to the baseline coefficients.

Retrieval of the vertical profiles of these molecules was carried out as described in Section 3. The OEM fit and the experimental data are presented in Fig. 6. The residuals around sharp spectral features of O_3 and N_2O in Fig. 6 show no evidence of frequency mismatch between the experimental and modeled spectra, lending confidence to the frequency calibration process. However, a systematic error in the fit that is larger than the system's random noise floor is observed between ~1160.8 and 1161.1 cm^{-1}, coinciding with the location of the broad CFC-12 absorption feature. This systematic error is common to all retrievals within this frequency range and is indicative of errors in the model, most likely arising from uncertainties in the absorption cross sections obtained from the HITRAN database [30]. The HITRAN cross section is provided with a frequency resolution >0.01 cm^{-1} for a coarse grid of temperatures and pressures. The low resolution of the database spectrum is expected to impact the accuracy of the atmospheric lineshape calculation, which reveals itself as mismatch between the modeled spectrum and the experimental spectrum collected with a higher spectral resolution of 0.002 cm^{-1}.

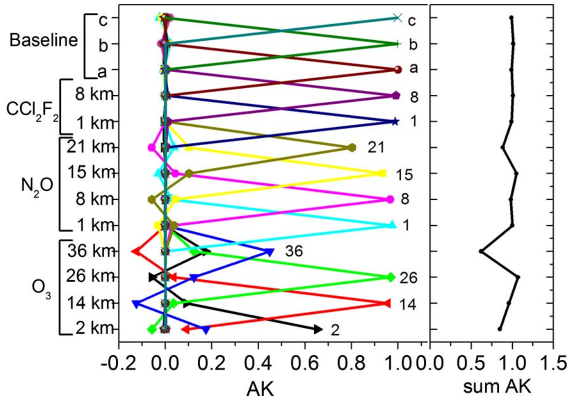

Fig. 7. (Color online) AK values for spectral window 2.

The AKs from the OEM fit to data in spectral window 2 are presented in Fig. 7. The peak values of AKs associated with the retrieval of the CFC-12 profile are close to one and are in good agreement with the expectations of the prior analysis calculations, lending confidence to the retrieved profiles. Concentrations of 500 ± 56 and 440 ± 42 pptv at altitudes of 1 and 8 km, respectively, are retrieved from the spectrum. Profiles of CFC-12 obtained in January 2007 from the Atmospheric Chemistry Experiment FTS [18] of the same absorption band at ~1161.0 cm^{-1} provided a CFC-12 concentration of approximately 500 to 560 pptv between 5 and 10 km. The retrievals from the EC-QC-LHR are in reasonably good agreement with this range of concentration levels.

C. Nitrous Oxide

Nitrous oxide was retrieved on an optimized grid of 1, 8, 15, and 21 km from a single absorption feature at 1161.48 cm^{-1} in spectral window 2 (Fig. 6). AK analysis (Fig. 7) indicates that there is little cross correlation between the retrieved N_2O parameters and other retrieved parameters, giving confidence to the

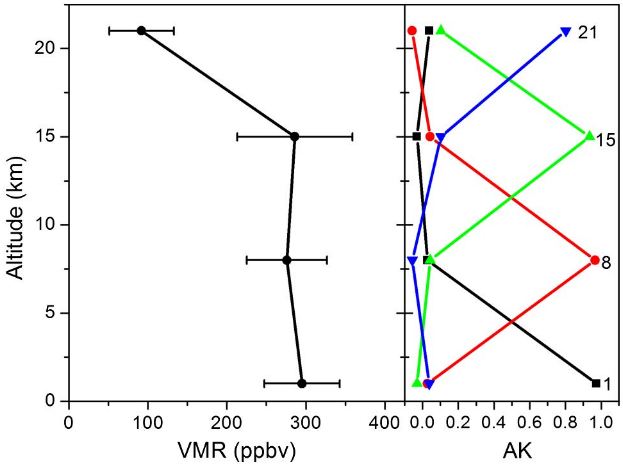

Fig. 8. (Color online) N_2O vertical profile retrieved from the single absorption line appearing in spectral window 2 (left) and the corresponding AK values (right).

validity of the retrieved profile presented in Fig. 8. The retrieved vertical profile shows a uniform concentration of around 300 ppbv in the troposphere from 1 to 15 km, with the concentration then dropping to approximately 100 ppbv at an altitude of 21 km. N_2O is well mixed in the troposphere, and our retrieved profile is consistent with profiles recorded by Fogal *et al.* with a high-resolution FTS instrument during the middle atmosphere nitrogen trend assessment (MANTRA) campaign over Vanscoy, Canada, in 1998 [36] and with measurements from ground-based FTS (MkIV), balloon sondes (MIPAS-B), and satellite sounder (ILAS-II) over Kiruna, Sweden, in 2003 [37]. In both measurement campaigns concentrations of 250 to 300 ppbv of N_2O at altitudes between ~10 and 15 km with a steady drop down to ~100 ppbv at ~25 km were measured. These measurements did not extend below 10 km, but ground-level observations at the Mace Head station in Northern Ireland recorded concentrations of nitrous oxide of 323 ppbv [38], which is within the retrieval errors estimated at 1 km altitude for the instrument discussed here.

D. Methane

Figure 9 presents the spectrum recorded between 1216.11 and 1216.76 cm^{-1}, which contains three CH_4 absorption lines. In addition to CH_4, there is also water vapor absorption, which contributes as a broadband feature throughout the spectral window with a weak absorption line that spectrally coincides with the CH_4 line at 1216.19 cm^{-1}. Retrievals of both methane and water vapor profiles have been performed, and the OEM fit to the experimental spectrum is shown in Fig. 9. Initially a full spectral range was used to perform retrieval, but inspection of the residuals to the OEM fit shows that the lineshapes for lines centered at 1216.19 and 1216.24 cm^{-1} are not well reproduced by the model. This is attributed to the following: (1) the water absorption line that spectrally overlaps with the methane line at 1216.19 cm^{-1} can obscure information pertaining to the CH_4 retrieval, and (2) the HITRAN air-broadening coefficient for the weak CH_4 line located at 1216.24 cm^{-1} is not well defined (noted as an average or estimation in the database [30]). Therefore similar to the ozone case (Section 4.A), this methane retrieval is repeated using a single methane line within a range of 1216.49 to 1216.75 cm^{-1} to mitigate the influences from model error and H_2O contribution. In this spectral range, the H_2O profile is not retrieved and is instead set equal to the vertical profile of water obtained from the ECMWF. The resulting profile of CH_4 and the corresponding AKs are presented in Fig. 10. The CH_4 AK peak values are close to one and show negligible correlation to baseline parameters (cross-correlation variance terms are <1%), which suggests that the information retrieved is derived from the measurement and not from the *a priori* values. Satellite (GOSAT) and ground-based FTS measurements (Total Carbon Column Observing Network [TCCON]) [39] along with airplane campaigns (HIPPO) [24] have demonstrated that methane concentrations of ~1.8 ppmv are evenly distributed in the troposphere, and at higher altitudes, MANTRA [36] shows that methane slightly decreases from ~1.7 ppm at 12 km to ~1.35 ppm at 20 km. Therefore, the retrieved concentrations from the EC-QC-LHR measurements are in good agreement with other observations.

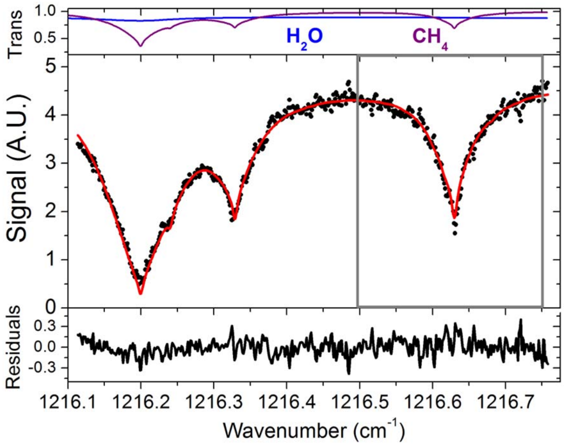

Fig. 9. (Color online) Spectral window 4. The top plot is an RFM simulation of the transmission spectrum for standard atmospheric conditions; the center plot is the experimental spectrum with the OEM fit overlaid; and the bottom plot shows the residual differences between the OEM fit and the data. The OEM fit is performed using a full range of spectral window 4. An improved retrieval is obtained for a reduced spectral range containing the single CH_4 line at 1216.6 cm^{-1}, as described in the text.

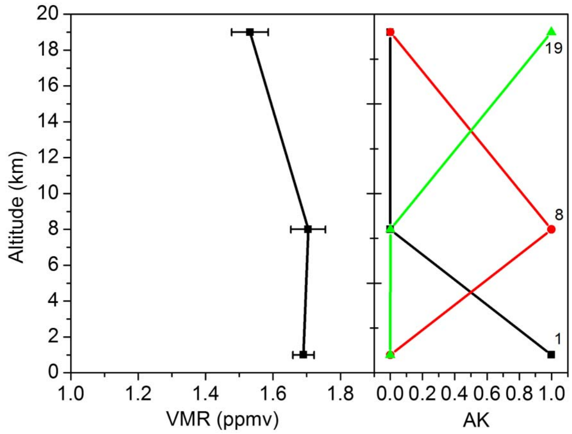

Fig. 10. (Color online) Methane vertical profile (left) retrieved from a truncated spectral range (1216.49–1216.75 cm^{-1}) containing a single isolated CH_4 line and AKs corresponding to the OEM fit (right).

E. Water

Water vapor absorption has been shown to contribute to all of the spectral windows of the EC-QC-LHR measurements presented so far. However, these H_2O features are broadband and often are strongly overlapped with absorption lines of other molecules. Therefore it is expected that only limited information about the water vertical profiles can be retrieved by

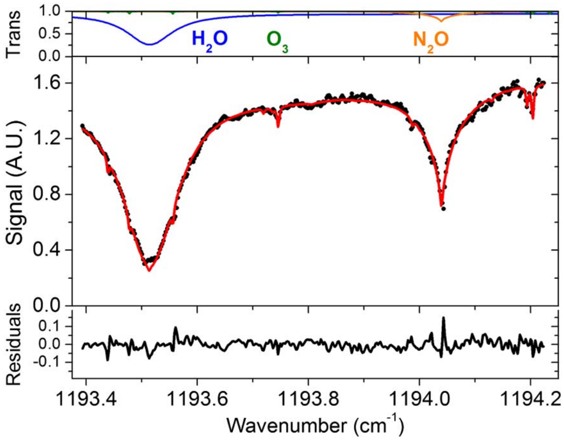

Fig. 11. (Color online) RFM simulation for standard atmospheric conditions (top plot), acquired spectral data shown as black dots and OEM fit shown as red line (center plot), and fit residuals (bottom plot) in spectral window 3.

EC-QC-LHR. To minimize retrieval error, the target water absorption feature should be an unsaturated, distinct, and narrow line rather than a broadband feature. For this reason, a water line centered at 1193.49 cm^{-1} that shows minimum spectral interference from other molecules was selected for further investigation. The upper section of Fig. 11 shows a spectrum simulated between 1193.39 and 1194.22 cm^{-1} that contains the target water vapor absorption line, an N_2O absorption line centered at 1194.04 cm^{-1}, and several weak O_3 absorption lines. The concentration profile of H_2O is retrieved on an optimized two-point altitude grid of 0.5 and 4 km, and the profile of N_2O concentration is retrieved on a grid of 1, 9, 15, and 22 km. The spectrum of ozone was generated using the fixed concentration profile obtained from ECMWF because no advantage was found in retrieving the profile. The OEM fit along with the residuals are shown in Fig. 11. The residuals are generally less than 5% of the maximum signal intensity. Because frequency calibration was performed using very weak O_3 absorption features available within the spectral scan, the accuracy of the calibration was reduced and slightly larger errors can be observed in the vicinity of narrow O_3 and N_2O lines. This however has negligible effect on the quality of the retrieval focused on the broadband H_2O feature.

The retrieved values for water vapor at 0.5 and 4 km are 3314 ± 247 and 81 ± 20 ppmv, respectively. Compared with the water profile retrieved from spectral window 1, there is no improvement in altitude grid, but the total retrieval error is significantly smaller in the case of spectral window 3. The concentration levels from the ECMWF-generated profile interpolated on the experimental altitude grid and vertical resolution provide comparable concentration levels of 3394 ppmv for the lower layer (within 0 to 2.5 km altitude defined by AKs), and 50 ppmv for the remaining layer (within 2.5 to 20 km altitude range). AK values at both 0.5 and 4 km altitude points are close to one and show little correlation (<2%) between the two altitudes, which indicates that the retrieved concentrations at the two altitudes can be attributed to the correct layer.

5. Comparison with FTS

To validate the EC-QC-LHR measurements and compare them to an instrument that is a well-established standard in radiometric sounding of atmospheric constituents [40], we performed a cross-validation measurement campaign with a Bruker IFS 125HR FTS. The FTS is capable of up to 0.0017 cm^{-1} (50 MHz) spectral resolution and has a physical footprint of 4 m × 2 m, which is approximately 12.5 times larger than the 0.8 m × 0.8 m footprint of EC-QC-LHR. With a KBr beam splitter and a liquid-nitrogen-cooled mercury cadmium telluride detector, the 3 dB optical frequency range of the FTS is 800 to 4000 cm^{-1}. The FTS shared the same FOV as the EC-QC-LHR (ensuring the same spatial resolution of the atmospheric observations), but only 50% of the solar intensity was directed toward the FTS instrument due to the insertion of a 50:50 beam splitter into the path of the solar radiation. A qualitative comparison of the FTS and the EC-QC-LHR spectra recorded with the same ultrahigh spectral resolution of 60 MHz (0.002 cm^{-1}) and the same coherent FOV was reported in [28]. It demonstrated that although the FTS spectrum was an average of 10 scans acquired over 2 h, the SNR was insufficient to observe all but the strongest absorption features (the SNR approximated for the strongest lines was as little as ~2.5). Therefore, the 60 MHz FTS data was deemed a poor prospect for retrieving atmospheric profiles, and no further analysis was carried out with these FTS spectra. In contrast, the EC-QC-LHR spectra acquired in 2 to 3 min had typical SNRs of 30 to 80, which is sufficient to observe multiple absorption features and could be used for atmospheric profiling, as shown in Section 4. FTS spectra with sufficient SNR to resolve absorption features were collected at a lower spectral resolution of 600 MHz (0.02 cm^{-1}) and with a larger aperture (2 mm). The measurements were collected on the 17 December 2010 and were an average of 60 scans acquired over 72 min. The SNR of the averaged spectrum was ~15 times higher than the SNR of FTS spectra recorded at 60 MHz resolution and therefore provides a good prospect for the retrieval of molecular profiles.

A side-by-side analysis of quality of the retrievals obtained from FTS and EC-QC-LHR measurements is beyond the scope of this manuscript and will be the subject of an independent publication. Nevertheless, to confirm the relevance of the EC-QC-LHR measurements, retrieval has been performed using a 100 cm^{-1} spectral window (1120–1220 cm^{-1}) of FTS data, which coincides with the frequency range of the EC-QCL. The altitudinal grids are the same for both instruments to allow straightforward comparison and are set equal to the grids in bold in Table 1. Prior

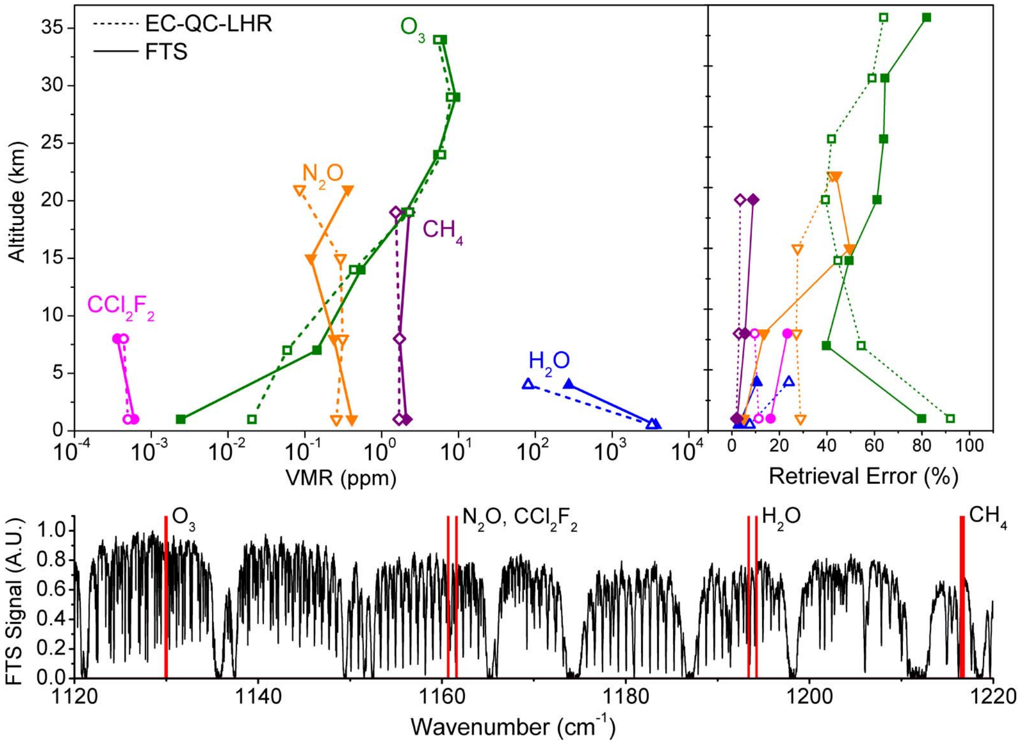

Fig. 12. (Color online) Comparison of vertical profiles (top left) and retrieval errors (top right) for all five target molecules retrieved from FTS data (solid lines, solid symbols) and from EC-QC-LHR spectral windows (dotted lines, open symbols). The spectral ranges of the two instruments are illustrated in the bottom plot, in which the FTS spectrum covers 1120 to 1220 cm^{-1} and the EC-QC-LHR spectral windows are noted by red vertical lines.

analysis of the FTS data indicate that the number of altitude points in the optimized altitudinal grids for the FTS retrievals are rather similar to those of the EC-QC-LHR: two fewer points for O_3, one additional point for N_2O and H_2O, and identical number of points for CH_4 and CFC-12. Over- or undersampling the altitude grid is reflected into the amount of retrieval smoothing noise and is therefore accounted for in this analysis. The same OEM algorithm with the Fourier transform of a medium Beer–Norton function as the ILS is used to retrieve vertical profiles from the FTS data [41].

The FTS retrieval results are shown in Fig. 12, plotted together with the EC-QC-LHR vertical profiles presented in Section 4. The profiles measured by both instruments show excellent agreement with the exception of the ozone data at ground level. At lower altitudes (<12 km), retrieval errors are generally smaller for the FTS than for the EC-QC-LHR (except for broadband CFC-12 and to a lesser extent for CH_4). At higher altitudes, the EC-QC-LHR measurements exhibit smaller errors owing to a higher spectral resolution. Considering that the FTS analysis is made over a frequency range of ~100 cm^{-1} with an acquisition time of ~1 h whereas EC-QC-LHR data are obtained from a single absorption line or doublet lying in a <1 cm^{-1} spectral span acquired in few minutes, the relevance of high temporal and spectral resolution EC-QC-LHR for atmospheric sounding is well illustrated by this retrieval comparison.

6. Conclusion

Following a solar occultation atmospheric measurement campaign in the United Kingdom during winter 2010/2011, high-resolution (60 MHz) spectra obtained from an EC-QC-LHR covering 118 cm^{-1} were analyzed to retrieve atmospheric profiles of five atmospherically important molecules. The use of EC-QCL as the LO offers a larger frequency range compared with other single-frequency laser sources, and simultaneous atmospheric observations of multiple species was successfully established. Using the OEM, vertical profiles of ozone, nitrous oxide, methane, CFC-12, and water vapor have been retrieved from ~1 cm^{-1} wide high-resolution (0.002 cm^{-1}) spectra that could be acquired anywhere within the available 118 cm^{-1} operational range of the instrument. The retrieved profiles are in good agreement with data from ECMWF (ozone and water), with measurements published in the literature (nitrous oxide, methane, and CFC-12), and with results obtained from spectra recorded by a high-resolution FTS during the same measurement campaign. The results demonstrate that QCL-based LHR is capable of performing thermal infrared sounding at sub-Doppler resolution, yielding robust retrieval of vertical profile information even from relatively narrow spectral scans covering sometimes only a single absorption line. Additionally the EC-QC-LHR temporal resolution for atmospheric profiling is demonstrated to be as high as few minutes, which is significantly better than what is achievable with FTS under the same condition of high spectral and spatial resolutions. A brief comparison between the EC-QC-LHR and a high-resolution FTS was presented to validate the measured profiles from independent high-resolution spectrometer data. It demonstrates good agreement between the retrieved profiles and confirms that EC-QC-LHR technology has great potential for providing reliable atmospheric sounding by a compact instrument with high spatial and temporal resolution capabilities. Yet a thorough comparison between the two instruments that fully exploits the ultrabroadband spectral coverage of the FTS is still ongoing and will be the subject of a future publication.

Although, due to current equipment limitations, this measurement campaign did not include any EC-QC-LHR spectral measurements taken over the entire available EC-QCL frequency range, it is possible to do so and to further improve the quality of the EC-QC-LHR retrieval. With an active wavelength-control technology developed recently for EC-QCLs [42], the LO wavelength can be step tuned over the entire EC-QCL frequency range while preserving the laser linewidth-limited high-spectral-resolution demonstrated with the mode-hop-free scan used in this work. Capabilities of this technology are very promising and will be explored in the future.

With work currently ongoing toward integration and miniaturization of QCL-based LHR, we foresee the advent of a thermal infrared sounder with high spectral resolution for high-vertical-resolution profiling in the nadir or zenith sounding modes. The high geographical resolution set by the coherent FOV (or a high vertical resolution in the limb sounding mode) and high temporal resolution on the order of minutes in a small and lightweight package is without precedent. A miniature QC-LHR would allow various options for deployment: on the ground in the form of a dense observation network of autonomous stations, on unmanned aerial vehicles for limb observations of the upper troposphere and lower stratosphere, or on forthcoming high-altitude platforms [43].

We acknowledge the ECMWF and the British Atmospheric Data Centre for providing the operational atmospheric profiles. This work was supported through the UK NERC research grant NE/H002383/1 and the UK STFC Innovation Ltd. proof-of-concept grant, by the U.S. National Science Foundation (NSF) Engineering Research Center Mid-InfraRed Technologies for Health and the Environment (MIRTHE), and the NSF Graduate Research Fellowship DGE-0646086. The authors wish to thank colleagues within RAL Space: Dr. Neil Macleod for assistance taking the FTS measurements and Gary Williams for his technical assistance.

References

1. R. T. Menzies, *Laser Monitoring of the Atmosphere*, E. D. Hinkley, ed. (Springer, 1976).
2. D. Weidmann, W. J. Reburn, and K. M. Smith, "Retrieval of atmospheric ozone profiles from an infrared quantum cascade laser heterodyne radiometer: results and analysis," Appl. Opt. **46**, 7162–7171 (2007).
3. D. Weidmann, W. J. Reburn, and K. M. Smith, "Ground-based prototype quantum cascade laser heterodyne radiometer for atmospheric studies," Rev. Sci. Instrum. **78**, 073107 (2007).
4. R. T. Menzies and R. K. Seals, "Ozone monitoring with an infrared heterodyne radiometer," Science **197**, 1275–1277 (1977).
5. M. A. Frerking and D. J. Muehlner, "Infrared heterodyne spectroscopy of atmospheric ozone," Appl. Opt. **16**, 526–528 (1977).
6. M. M. Abbas, T. Kostiuk, M. J. Mumma, D. Buhl, V. G. Kunde, and L. W. Brown, "Stratospheric ozone measurement with an infrared heterodyne spectrometer," Geophys. Res. Lett. **5**, 317–320 (1978).
7. F. Allario, J. Hoell, S. Katzberg, and J. Larsen, "An experiment concept to measure stratospheric trace constituents by laser heterodyne spectroscopy," Appl. Phys. A **23**, 47–56 (1980).
8. H. Fukunishi, S. Okano, M. Taguchi, and T. Ohnuma, "Laser heterodyne spectrometer using a liquid nitrogen cooled tunable diode laser for remote measurements of atmospheric O_3 and N_2O," Appl. Opt. **29**, 2722–2728 (1990).
9. W. Bell, N. A. Martin, T. D. Gardiner, N. R. Swann, P. T. Woods, P. F. Fogal, and J. W. Waters, "Column measurements of stratospheric trace species over Åre, Sweden in the winter of 1991–1992," Geophys. Res. Lett. **21**, 1347–1350 (1994).
10. D. Weidmann and G. Wysocki, "High-resolution broadband (>100 cm^{-1}) infrared heterodyne spectro-radiometry using an external cavity quantum cascade laser," Opt. Express **17**, 248–259 (2009).
11. D. Weidmann, B. J. Perrett, N. A. Macleod, and R. M. Jenkins, "Hollow waveguide photomixing for quantum cascade laser heterodyne spectro-radiometry," Opt. Express **19**, 9074–9085 (2011).
12. D. Stupar, J. Krieg, P. Krötz, G. Sonnabend, M. Sornig, T. F. Giesen, and R. Schieder, "Fully reflective external-cavity setup for quantum-cascade lasers as a local oscillator in mid-infrared wavelength heterodyne spectroscopy," Appl. Opt. **47**, 2993–2997 (2008).
13. C. Gmachl, D. L. Sivco, R. Colombelli, F. Capasso, and A. Y. Cho, "Ultra-broadband semiconductor laser," Nature **415**, 883–887 (2002).
14. A. Hugi, R. Terazzi, Y. Bonetti, A. Wittmann, M. Fischer, M. Beck, J. Faist, and E. Gini, "External cavity quantum cascade laser tunable from 7.6 to 11.4 μm," Appl. Phys. Lett. **95**, 061103–061103 (2009).
15. A. Wittmann, Y. Bonetti, M. Fischer, J. Faist, S. Blaser, and E. Gini, "Distributed-feedback quantum-cascade lasers at 9 μm operating in continuous wave up to 423 K," IEEE Photon. Technol. Lett. **21**, 814–816 (2009).
16. P. L. Kinney, "The pulmonary effects of outdoor ozone and particle air pollution," Semin. Respir. Crit. Care Med. **20**, 601–607 (1999).
17. Montreal Protocol on Substances that Deplete the Ozone Layer (United Nations Environment Programme, 2009).
18. E. Mahieu, P. Duchatelet, P. Demoulin, K. A. Walker, E. Dupuy, L. Froidevaux, C. Randall, V. Catoire, K. Strong, C. D. Boone, P. F. Bernath, J.-F. Blavier, T. Blumenstock, M. Coffey, M. De Mazière, D. Griffith, J. Hannigan, F. Hase, N. Jones, K. W. Jucks, A. Kagawa, Y. Kasai, Y. Mebarki, S. Mikuteit, R. Nassar, J. Notholt, C. P. Rinsland, C. Robert, O. Schrems, C. Senten, D. Smale, J. Taylor, C. Tétard, G. C. Toon, T. Warneke, S. W. Wood, R. Zander, and C. Servais, "Validation of ACE-FTS v2.2 measurements of HCl, HF, CCl_3F and CCl_2F_2 using space-, balloon- and ground-based instrument observations," Atmos. Chem. Phys. **8**, 6199–6221 (2008).
19. C. P. Rinsland, C. Boone, R. Nassar, K. Walker, P. Bernath, E. Mahieu, R. Zander, J. C. McConnell, and L. Chiou, "Trends of HF, HCl, CCl_2F_2, CCl_3F, $CHClF_2$ (HCFC-22), and SF_6 in the lower stratosphere from atmospheric chemistry experiment (ACE) and atmospheric trace molecule spectroscopy (ATMOS) measurements near 30°N latitude," Geophys. Res. Lett. **32**, L16S03 (2005).
20. T. R. Karl and K. E. Trenberth, "Modern global climate change," Science **302**, 1719–1723 (2003).

21. Kyoto Protocol to the United Nations Framework Convention on Climate Change (United Nations, 1998).
22. J. H. Seinfeld and S. N. Pandis, *Atmospheric Chemistry and Physics*, 2nd ed. (John Wiley & Sons, 2006).
23. D. R. Bates and P. B. Hays, "Atmospheric nitrous oxide," Planet. Space Sci. **15**, 189–197 (1967).
24. S. C. Wofsy, "HIAPER pole-to-pole observations (HIPPO): fine-grained, global-scale measurements of climatically important atmospheric gases and aerosols," Phil. Trans. R. Soc. A **369**, 2073–2086 (2011).
25. G. P. Brasseur, J. J. Orlando, and G. S. Tyndall, eds., *Atmospheric Chemistry and Global Change*, Topics in Environmental Chemistry (Oxford University, 1999).
26. D. J. Wuebbles and K. Hayhoe, "Atmospheric methane and global change," Earth-Sci. Rev. **57**, 177–210 (2002).
27. K. Trenberth, J. Fasullo, and L. Smith, "Trends and variability in column-integrated atmospheric water vapor," Clim. Dyn. **24**, 741–758 (2005).
28. D. Weidmann, T. Tsai, N. A. Macleod, and G. Wysocki, "Atmospheric observations of multiple molecular species using ultra-high-resolution external cavity quantum cascade laser heterodyne radiometry," Opt. Lett. **36**, 1951–1953 (2011).
29. G. Wysocki, R. F. Curl, F. K. Tittel, R. Maulini, J. M. Bulliard, and J. Faist, "Widely tunable mode-hop free external cavity quantum cascade laser for high resolution spectroscopic applications," Appl. Phys. B **81**, 769–777 (2005).
30. L. S. Rothman, I. E. Gordon, A. Barbe, D. C. Benner, P. F. Bernath, M. Birk, V. Boudon, L. R. Brown, A. Campargue, J. P. Champion, K. Chance, L. H. Coudert, V. Dana, V. M. Devi, S. Fally, J. M. Flaud, R. R. Gamache, A. Goldman, D. Jacquemart, I. Kleiner, N. Lacome, W. J. Lafferty, J. Y. Mandin, S. T. Massie, S. N. Mikhailenko, C. E. Miller, N. Moazzen–Ahmadi, O. V. Naumenko, A. V. Nikitin, J. Orphal, V. I. Perevalov, A. Perrin, A. Predoi–Cross, C. P. Rinsland, M. Rotger, M. Simecková, M. A. H. Smith, K. Sung, S. A. Tashkun, J. Tennyson, R. A. Toth, A. C. Vandaele, and J. Vander Auwera, "The HITRAN 2008 molecular spectroscopic database," J. Quant. Spectrosc. Radiat. Transfer **110**, 533–572 (2009).
31. C. D. Rodgers, *Inverse Methods for Atmospheric Sounding: Theory and Practice*, Atmospheric, Oceanic and Planetary Physics (World Scientific, 2000), Vol. **2**.
32. A. Dudhia, "Reference forward model software user's manual," http://www.atm.ox.ac.uk/RFM/sum.
33. European Centre for Medium-Range Weather Forecasts, "ECMWF data archive services," http://www.ecmwf.int/products/data/archive/.
34. D. McNaughton, D. McGilvery, and E. G. Robertson, "High-resolution FTIR-jet spectroscopy of CCl_2F_2," J. Chem. Soc. Faraday Trans. **90**, 1055–1060 (1994).
35. M. Morillon–Chapey, A. O. Diallo, and J. C. Deroche, "Isotopic and vibrational assignments of fluorocarbon-12 in the 8.6 μm and 10.8 μm regions," J. Mol. Spectrosc. **88**, 424–427 (1981).
36. P. F. Fogal, R. D. Blatherwick, F. J. Murcray, and J. R. Olson, "Infra-red FTS measurements of CH_4, N_2O, O_3, HNO_3, HCl, CFC-11 and CFC-12 from the MANTRA balloon campaign," Atmos. Ocean **43**, 351–359 (2005).
37. M. K. Ejiri, Y. Terao, T. Sugita, H. Nakajima, T. Yokota, G. C. Toon, B. Sen, G. Wetzel, H. Oelhaf, J. Urban, D. Murtagh, H. Irie, N. Saitoh, T. Tanaka, H. Kanzawa, M. Shiotani, S. Aoki, G. Hashida, T. Machida, T. Nakazawa, H. Kobayashi, and Y. Sasano, "Validation of the improved limb atmospheric spectrometer-II (ILAS-II) version 1.4 nitrous oxide and methane profiles," J. Geophys. Res. **111**, D22S90 (2006).
38. R. G. Prinn, R. F. Weiss, P. J. Fraser, P. G. Simmonds, S. O'Doherty, P. Salameh, L. Porter, P. Krummel, R. H. J. Wang, B. R. Miller, C. Harth, B. Greally, F. A. Van Woy, L. P. Steele, J. Muehle, G. Sturrock, F. N. Alyea, J. Huang, and D. E. Hartley, "The ALE/GAGE/AGAGE network," http://cdiac.ornl.gov/ndps/alegage.html.
39. R. Parker, H. Boesch, A. Cogan, A. Fraser, L. Feng, P. I. Palmer, J. Messerschmidt, N. Deutscher, D. W. T. Griffith, J. Notholt, P. O. Wennberg, and D. Wunch, "Methane observations from the greenhouse gases observing SATellite: Comparison to ground-based TCCON data and model calculations," Geophys. Res. Lett. **38**, L15807 (2011).
40. G. Toon, J. F. Blavier, R. Waschenfelder, D. Wunsch, G. Keppel–Aleks, P. Wennberg, B. Connor, V. Sherlock, D. Griffith, N. Deutscher, and J. Notholt, "Total column carbon observing network (TCCON)," in *Fourier Transform Spectroscopy*, OSA Technical Digest (Optical Society of America, 2009), JMA3.
41. R. H. Norton and R. Beer, "New apodizing functions for Fourier spectrometry," J. Opt. Soc. Am. **66**, 259–264 (1976).
42. T. Tsai and G. Wysocki, "Active wavelength control of an external cavity quantum cascade laser," Appl. Phys. B **109**, 415–421 (2012).
43. P. Edin, *Assessment of High Altitude Long Endurance (HALE) Platforms* (European Space Agency, 1998).